Journal of
Mechanics of
Materials and Structures

ANISOTROPIC STRESS STATE AROUND INTERNALLY PRESSURIZED MICROCHANNELS

Yong Xue Gan

Volume 3, Nº 2 February 2008

mathematical sciences publishers

JOURNAL OF MECHANICS OF MATERIALS AND STRUCTURES
Vol. 3, No. 2, 2008

ANISOTROPIC STRESS STATE AROUND INTERNALLY PRESSURIZED MICROCHANNELS

YONG XUE GAN

This work derives internal pressure induced stresses in material imbedded with square-shaped microchannels. The first part provides background on microchanneled materials at micro and nanoscale to motivate investigating the stress and deformation states. The second part develops a simplified model to characterize the plastic flow and/or motion of dislocations within crystalline, microchanneled materials. The model helps identify slip bands around the channels under plane strain deformation conditions. The third part derives solutions to the stress states around the microchannels, obtaining closed form solutions which hold for regions containing and away from the channel boundary. Figures depict the stress solutions in both physical and stress space. The results predict nonuniform deformation states around the channels and also reveal the yield conditions associated with the plastic flow along different slip bands. The work concludes with case studies on the stress states of microneedles containing square microchannels for applications such as fluid injection, nanofiber growth, and cell registration.

1. Introduction

Microchannels and arrays of channels function as important components in many microscale and nanoscale systems [Allen 2005]. For example, microchannels and their arrays can be fabricated for molecular sieves, particle filters, capillary pores, or nutrient delivery units. Microchannels have also been used for chemical reaction flow beds, nanoimprinting molds, ink jets, and templates for synthesis of nanofibers. Fabrication technology for microfluidic channels has been extensively studied [Franssila 2004]. To make a microchannel, it is very common to sandwich a sacrificial photoresist layer between two layers. Supporting posts may be added into the photoresist to allow larger embedded features, as shown by Hwang and Song [2007]. After photolithography, microchannels form from selective dissolution of the photoresist [Senturia 2001].

Many publications explore new technology for fabricating microchannels. A three dimensional manufacturing process has been developed to make embedded microchannels using scanning laser systems, as shown by Lee et al. [2003], Li et al. [2004], Yu et al. [2004], Yu et al. [2006a], and Yu et al. [2006b]. The authors discussed potential ways to manipulate and position cells using suction forces. Recently, Ziegler et al. [2006] fabricated neural probes with built-in microfluidic channels by micromolding and thermal bonding of Parylene without using a photoresist. The probes containing the fluidic channels were tested for delivering small amounts of drugs into biological tissue as well as for neural recording.

Keywords: microchannel, anisotropic deformation, stress field, plastic flow, nanocrystalline material.
This work is supported by The Durbin Faculty Development Grant from The Cooper Union for the Advancement of Science and Art.

One issue confronting microchannels is mechanical deformation. Engineers must ensure that the channels maintain a constant size, even as they are put through the rigors of their various applications. For microchannels used for inkjet printing, biofluid printing, fuel injection, drug delivery, or integrated circuits (IC), dimensional stability requires good cooling. A constant size is also required to successfully register a single cell in a microwell or channel. And, when using microchannels for bioparticle registration [Zhe et al. 2007] or microinjection [Lu et al. 2007], controlling their size is necessary for accurate counting or medicine delivery.

Microchannels in devices such as microfluid droplet injectors are typically under under both thermal and internal compressive loads, as addressed by Tseng et al. [2002a] and Tseng et al. [2002b]. These loads can cause single channels to deform in a way the could significantly influence the performance of the entire channel array structure, in view of hydraulic cross-talk, flow resistance and fluid accumulation. In microfluidic devices, the stresses around the microchannels come from other sources, such as fluid pressure, electric potential, van der Waals, and capillary forces. Sidewall contact friction, as described by Timpe and Komvopoulos [2006], may also cause the stresses to redistribute around the microchannels. Predicting the deformation state around a microchannel requires determining the stress field.

The problem of microcavities in isotropic plastic materials has caught much attention because of their importance in fracture mechanics. For example, Tvergaard and Hutchinson [2002] analyzed numerically a two-dimensional plane strain model with multiple discrete cavities and found that cavity interaction determines the threshold for crack initiation and their resistance to growth. Lubarda et al. [2004] studied how cavities grow by emitting dislocations and proposed an onset criterion for such events at the surface of a cavity under remote tension. They also calculated, for any initial cavity size, the critical stress for emitting a single dislocation or a dislocation pair. They found that the critical stress decreases with increasing cavity size and also found that dislocations with a wider core are more likely to be emitted than ones with a narrow core.

Many factors influence the growth of cavities in elastic-plastic crystalline solids, for example, plastic anisotropy [O'Regan et al. 1997] and crystallographic orientation [Schacht et al. 2003]. The length-scale effect in plastic deformation has also been found in the growth of microcavities [Fleck et al. 1994]; the nonlocal elastic-plastic material model reveals that the rate of cavity growth decreases significantly when the cavities are shrunk to sizes approaching the characteristic length of the material [Tvergaard and Niordson 2004]. The cavity size distribution also affects the crack growth rate [Needleman and Tvergaard 1991]. Huang et al. [1991] and Tvergaard [1991] have addressed cavitation instabilities in elastic-plastic solids.

Using the formalism of anisotropic slip line theory, Kysar et al. [2005] derived the stress state in a cylindrical void due to far-field external compression. In recent work [Gan and Kysar 2007], we presented the solutions to the stresses from both internal pressure and far-field loading. In addition, we obtained experimental and simulation results to validate the theory predicting the deformed state in materials containing microcavities [Gan et al. 2006]. In fabricating microelectromechanical systems (MEMS) and nanoelectromechanical systems (NEMS) in single crystalline materials such as Si, Cu, Ni, Ag, Au, and Pd, sharp-cornered channels may form because of anisotropic etching [Senturia 2001]. Understanding the deformation of materials containing such channels — which will entail studying the anisotropic stress states around them — will be helpful for MEMS and NEMS design.

This work uses a simplified plastic flow model to derive stresses near square-shaped microchannels. We determine slip bands around the channels in materials under plane strain deformation conditions and establish different stress zones associated with the active slip of two systems. We derive closed-form solutions in stress zones that either contain or are away from the channel inner boundary. The stress solutions are plotted in both physical space and stress space. The results will be used to analyze the deformation state around the microchannels. Finally, we give stress maps of microneedles containing square shaped microchannels.

2. Plasticity analysis

2.1. ***Slip model.*** If the matrix material containing microchannels has a well defined yield point, the plastic flow analysis of Nadai [1950] will determine the stress state in the infinitesimal control volume containing the boundary point O shown in Figure 1a. Define x-y coordinates so that the x-axis is parallel to the internal pressure. Also define local ξ-η coordinates so the ξ-axis follows the plastic flow. The ξ-η coordinates define the principal stresses of the problem. The maximum normal stress σ_m is parallel to the η-axis, and the maximum shear stress τ_m is along the ξ-axis.

Assuming that the angle between x and ξ is ϕ, the principal stress components are

$$\sigma_m = -\frac{p}{2}\left[1-\cos(2\phi)\right], \qquad \tau_m = -\frac{p}{2}\sin(2\phi).$$

Define $-\epsilon_{xx}$ as the compressive plastic strain in the η direction. Assuming incompressibility, the materials expands in all other directions, and the magnitude of strain due to the expansion must be $\epsilon_{xx}/2$. If the pressure along the entire boundary NT is uniform, as shown in Figure 1b, the normal strain along the

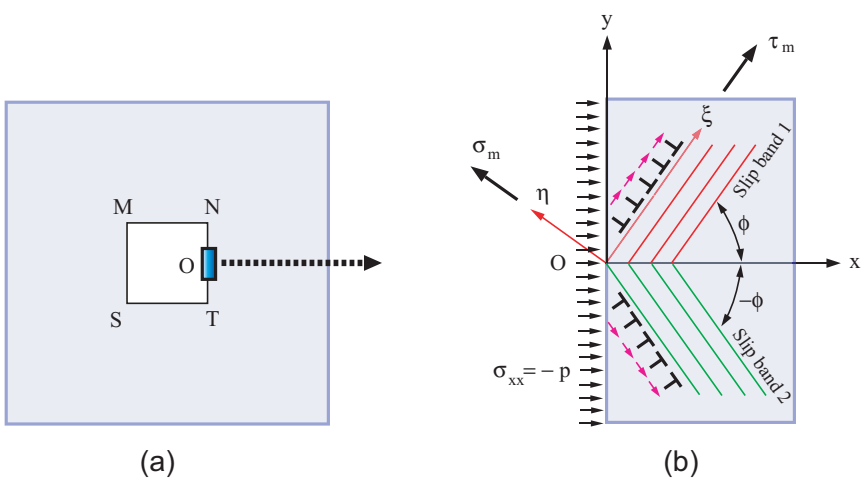

Figure 1. Schematic of a microchannel and the deformation state: (a) square microchannel, (b) magnified region around point O showing the slip in the material under internal pressure.

η-axis, ϵ_m, and the shear strain along the ξ-axis, γ_m, are

$$\epsilon_m = \frac{\epsilon_{xx}}{4}\left[1 + 3\cos(2\phi)\right], \qquad \gamma_m = \frac{3\epsilon_{xx}}{4}\sin(2\phi).$$

In this problem, we consider slip to be the major plastic deformation mechanism. The plastic flow along the ξ-axis results in vanishing net normal strain, that is

$$\epsilon_m = \frac{\epsilon_{xx}}{4}\left[1 + 3\cos(2\phi)\right] = 0,$$

from which $\cos(2\phi) = -1/3$ and $\phi = 54.7°$. By symmetry, another solution $\phi = -54.7°$ holds in the quadrant with $y < 0$ and $x > 0$, as schematically shown in Figure 1b. Also by symmetry, we obtain the distribution of all the slip bands around the microchannel, as shown in Figure 2. From Figure 2, only one slip band exists in each half-quadrant, that is, only one slip system is active. For example, in the angular region $0 \le \theta \le \pi/4$, slip system 1 is active, while in $\pi/4 \le \theta \le \pi/2$, only slip system 2 is active, and so forth. According to Rice [1973], if the single slip condition holds, the two families of slip lines form mutually orthogonal nets. Slip lines parallel to the slip direction are defined as α-lines; and those normal to the slip plane are called β-lines. In this case, the α-lines are along the ξ-axis, while the β-lines are along the η-axis.

2.2. ***Yield surface.*** Schmid's Law for a single split system describes the state just before it yields:

$$\mathbf{n} \cdot \Sigma \cdot \mathbf{s} = \pm\tau, \tag{1}$$

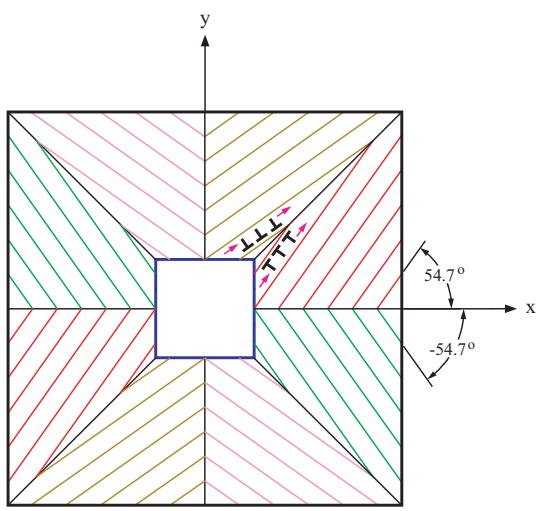

Figure 2. Illustration of the slip bands around the microchannel.

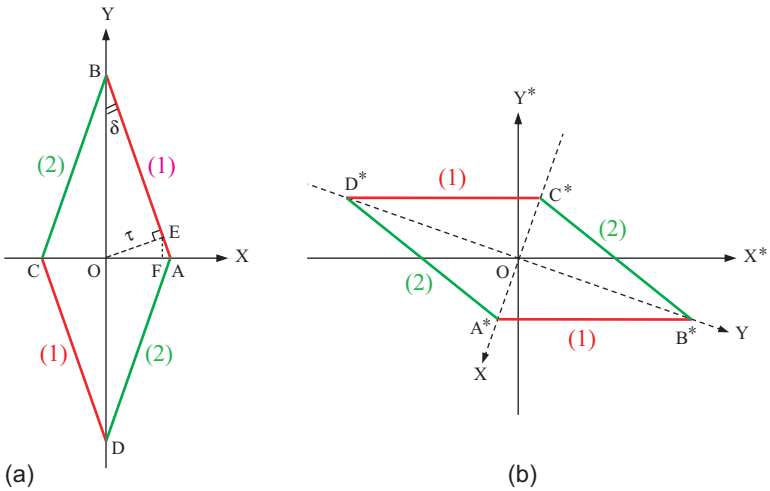

Figure 3. Yield surface associated with the two active slip systems: (a) yield surface without rotation, (b) rotated yield surface.

where τ is the shear strength, $\mathbf{n}$ is the surface normal of the slip plane, $\mathbf{s}$ is a unit vector along the slip direction, and Σ is the stress tensor given in rectangular coordinates as

$$\Sigma = \begin{pmatrix} \sigma_{xx} & \sigma_{xy} & \sigma_{xz} \\ \sigma_{yx} & \sigma_{yy} & \sigma_{yz} \\ \sigma_{zx} & \sigma_{zy} & \sigma_{zz} \end{pmatrix}. \tag{2}$$

We denote the rectangular components of $\mathbf{n}$ and $\mathbf{s}$ by (s_x, s_y, s_z) and (n_x, n_y, n_z). Because we consider here deformation under the plane strain conditions, the slip occurs within the x-y plane, and $s_z = 0$. For the plane strain state, $\sigma_{xz} = \sigma_{zx} = 0$ and $\sigma_{yz} = \sigma_{zy} = 0$. Also, because the stress tensor is symmetric, $\sigma_{xy} = \sigma_{xy}$.

Fully written out in components, Equation (1) reads

$$n_x\sigma_{xx}s_x + n_y\sigma_{yx}s_x + n_x\sigma_{xy}s_y + n_y\sigma_{yy}s_y = \pm\tau,$$

or, rearranging,

$$n_x s_x\sigma_{xx} + n_y s_y\sigma_{yy}s + (n_x s_y + n_y s_x)\sigma_{yx} = \pm\tau.$$

The components of $\mathbf{s}$ and $\mathbf{n}$ are expressed in the slip angle ϕ as

$$\begin{aligned} s_x &= \cos\phi, & s_y &= \sin\phi, \\ n_x &= -s_y = -\sin\phi, & n_y &= s_x = \cos\phi, \end{aligned}$$

and the yield condition becomes either of

$$\sin(2\phi)\frac{\sigma_{xx} - \sigma_{yy}}{2} + \cos(2\phi)\sigma_{xy} = \pm\tau \qquad \text{or} \qquad \sigma_{xy} = \tan(2\phi)\frac{\sigma_{xx} - \sigma_{yy}}{2} \pm \frac{\tau}{\cos(2\phi)}. \tag{3}$$

Let $X = (\sigma_{xx} - \sigma_{yy})/2$ and $Y = \sigma_{xy}$. The yield functions as defined by Equation (3) can be plotted in the stress space or Π-plane with X as the abscissa and Y as the axis. The function can be used to

Vertex	A	B	C	D
$X\left(\dfrac{\sigma_{xx}-\sigma_{yy}}{2\tau}\right)$	$\dfrac{3\sqrt{2}}{4}$	0	$-\dfrac{3\sqrt{2}}{4}$	0
$Y\left(\dfrac{\sigma_{xy}}{\tau}\right)$	0	3	0	-3

Table 1. Yield surface vertices on (left) X-Y plane and (right) the X^*-Y^* plane.

define a yield surface shown in Figure 3a and derived as follows. Obviously, two parallel lines define the yield condition for the active slip of slip system 1 with the angle ϕ. The slope of the two lines is $\tan(2\phi)$, and the two lines intercept the Y-axis at $\pm\tau/\cos(2\phi)$. Similarly, for the slip system with the slip angle $-\phi$, slip system 2, the yield surfaces are represented by another two lines with slope $-\tan(2\phi)$ and intercepting the Y-axis at $\pm\tau/\cos(2\phi)$. Altogether, these four lines draw the diamond shape shown in the figure. Table 1 lists the coordinates of the diamond's vertices.

In a local ξ-η coordinate system with the ξ-axis along the slip direction **s** and the η-axis along the slip plane normal **n**, the yield surface is obtained by rotating clockwise by 2ϕ the original yield surface in the Π-plane. Figure 3b shows the rotated yield surface plotted on the Π^*-plane with X^* as the abscissa and Y^* as the axis. Table 2 lists the vertices.

We will use these results from the analysis of yielding for solving the stresses in Section 3.

3. Stress field solution

3.1. ***Boundary condition.*** Because the inner surface of the microchannel is under compression, we have at point O that $\sigma_{xx} = -p$, where p is the internal pressure. As an approximation, we assume that this boundary condition propagates into the inner vertical wall of the channel. We assume that $\sigma_{xy} = 0$ on the inner wall because the free surface condition holds. However, σ_{yy} needs to be determined from the yield conditions. We note that the sign before τ in the right hand sides of Equation (3) should be positive because the compressive state inside the channel implies $(\sigma_{xx} - \sigma_{yy})/2 < 0$. Thus, the stress state at point O in the x-y physical space corresponds to point C in the X-Y stress space.

Vertex	A*	B*	C*	D*
$X^*\left(\dfrac{\sigma_{xx}-\sigma_{yy}}{2\tau}\right)$	$-\dfrac{1}{2\sqrt{2}}$	$2\sqrt{2}$	$\dfrac{1}{2\sqrt{2}}$	$-2\sqrt{2}$
$Y^*\left(\dfrac{\sigma_{xy}}{\tau}\right)$	-1	-1	1	1

Table 2. Yield surface vertices on the X^*-Y^* plane.

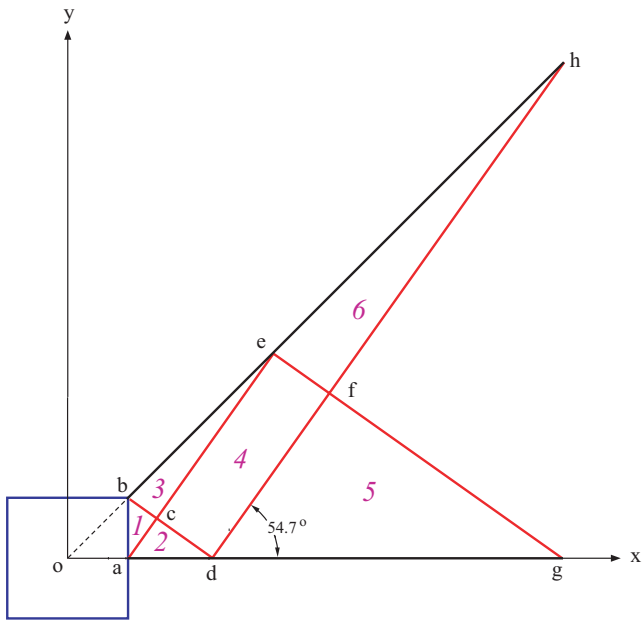

Figure 4. Typical stress zones in the angular region $0 \le \theta \le \pi/4$.

Once the sign before τ in Equation (3) is known, the stress component σ_{yy} can be found from a simplified yield condition, that is,

$$\sigma_{xy} = \tan(2\phi)\frac{\sigma_{xx} - \sigma_{yy}}{2} + \frac{\tau}{\cos(2\phi)}.$$

Substituting σ_{xx} and σ_{xy} into this equation and solving for σ_{yy} yields

$$\sigma_{yy} = \frac{\tau}{\sin(2\phi)} - p.$$

Therefore, the boundary conditions can be expressed as

$$\sigma_{xx} = -p, \qquad \sigma_{yy} = \frac{\tau}{\sin(2\phi)} - p, \qquad \sigma_{xy} = 0.$$

In polar coordinates, the stress components on the boundary are

$$\sigma_{rr} = \sigma_{xx}\cos^2\theta + \sigma_{yy}\sin^2\theta + \sigma_{xy}\sin(2\theta) = \frac{2\tau\sin^2\theta}{\sin(2\phi)} - p,$$

$$\sigma_{\theta\theta} = \sigma_{xx}\sin^2\theta + \sigma_{yy}\cos^2\theta - \sigma_{xy}\sin(2\theta) = \frac{2\tau\cos^2\theta}{\sin(2\phi)} - p,$$

$$\sigma_{r\theta} = -\frac{1}{2}(\sigma_{xx} - \sigma_{yy})\sin(2\theta) + \sigma_{xy}\cos(2\theta) = \frac{\tau\sin(2\theta)}{\sin(2\phi)}.$$

Vertex	x-position	y-position
a	1	0
b	1	1
c	$1+\sqrt{2}/3$	$2/3$
d	$1+\sqrt{2}$	0
e	$2+\sqrt{2}$	$2+\sqrt{2}$
f	$2+5\sqrt{2}/3$	$4/3+\sqrt{2}$
g	$4+3\sqrt{2}$	0

Table 3. Stress zone vertices.

3.2. ***Stress zones.*** The analysis of plastic flow and slip band in Section 2.1 implies the region around the microchannel can be divided into discrete zones as shown in Figure 4. In each zone, the stresses show similar properties. For example, in stress zone 1, the stresses are influenced by the boundary conditions given in Section 3.1. Stress zone 2 is adjacent to stress zone 1, and all the points in the two zones share the same β-line. Stress zone 3 is also adjacent to stress zone 1, but all the points in these two zones share the same α-line. Stress zone 4 is bounded by two α-lines (ce and df) and two β-lines (cd and ef). Additional stress zones such as stress zone 5 and stress zone 6 can be defined, as illustrated in Figure 4. For convenience, Table 3 lists the vertex coordinates in these stress zones.

3.3. ***Stress zone 1.*** Suppose that R_1 is an arbitrary point within stress zone 1. The α-line passing through R_1 intercepts the inner boundary of the microchannel at point P_1, while the β-line intercepts the inner

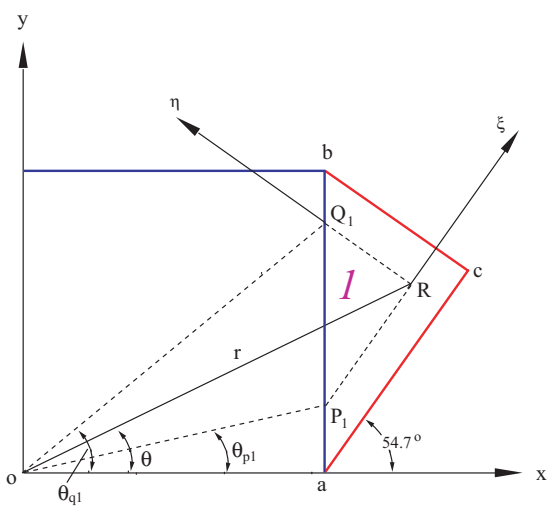

Figure 5. Drawing for finding stress in stress zone 1.

boundary at point Q_1, as shown in Figure 5. At the boundary points P_1 and Q_2, the stress states are

$$\text{at } P_1: \begin{cases} \sigma_{rr} = \dfrac{2\tau \sin^2 \theta_{p1}}{\sin(2\phi)} - p, \\ \sigma_{\theta\theta} = \dfrac{2\tau \cos^2 \theta_{p1}}{\sin(2\phi)} - p, \\ \sigma_{r\theta} = \dfrac{\tau \sin(2\theta_{p1})}{\sin(2\phi)}, \end{cases} \qquad \text{at } Q_1: \begin{cases} \sigma_{rr} = \dfrac{2\tau \sin^2 \theta_{q1}}{\sin(2\phi)} - p, \\ \sigma_{\theta\theta} = \dfrac{2\tau \cos^2 \theta_{q1}}{\sin(2\phi)} - p, \\ \sigma_{r\theta} = \dfrac{\tau \sin(2\theta_{q1})}{\sin(2\phi)}, \end{cases}$$

where θ_{p1} and θ_{q1} are defined as in Figure 5.

Now define a local ξ-η coordinate system with its ξ-axis along the α-line and the η-axis along the β-line for the split system with slip angle $\phi = 54.7°$. By applying the slip line theory as developed by Hill [1998] and Rice and Tracey [1969], the stress component $\sigma_{\xi\xi}$ in these coordinates is, at point R_1, the same as at point P_1, while $\sigma_{\eta\eta}$ at point R_1 equals that at Q_1. This is because the equilibrium equations are satisfied just before yielding. If there is no body force, the equilibrium conditions in the two dimensional Cartesian coordinate x-y system are

$$\frac{\partial \sigma_{xx}}{\partial x} + \frac{\partial \sigma_{xy}}{\partial y} = 0, \qquad \frac{\partial \sigma_{yx}}{\partial x} + \frac{\partial \sigma_{yy}}{\partial y} = 0.$$

Because the equilibrium must be satisfied for the entire stress zone, it is possible to seek a solution along the characteristics that are the anisotropic slip line traces, as mentioned before. Therefore, we are ready to determine the relationship among stress components along the α-line or β-line. If a new ξ-η coordinate system is chosen so that ξ and η coincide with the α-line and the the β-line, $\sigma_{\xi\eta} = \sigma_{\eta\xi} = \tau$ holds in the initial stage of yielding, with τ being the critical shear stress for the active slip system. This ignores any strain hardening effect. The equilibrium conditions in the local ξ-η coordinate system are

$$\frac{\partial \sigma_{\xi\xi}}{\partial \xi} = 0, \qquad \frac{\partial \sigma_{\eta\eta}}{\partial \eta} = 0.$$

The solutions of characteristics are

$$\begin{aligned} &\sigma_{\xi\xi} = \sigma_{\xi\xi}(\xi_1, \eta_1) \quad \text{along the } \alpha\text{-line: } \frac{dy}{dx} = \tan\phi, \\ &\sigma_{\eta\eta} = \sigma_{\eta\eta}(\xi_2, \eta_2) \quad \text{along the } \beta\text{-line: } \frac{dy}{dx} = -\cot\phi, \\ &\sigma_{\xi\eta} = \sigma_{\eta\xi} = \tau \qquad \text{along both the } \alpha\text{- and } \beta\text{-lines,} \end{aligned} \tag{4}$$

where ϕ is the slip angle, (ξ_1, η_1) and (ξ_2, η_2) are boundary points, and P_1 and Q_1 are associated with the α-line and β-line, respectively. Using this, the yield conditions, and the related boundary conditions, the stress state in stress zone 1 at the initial stage of plastic deformation can be fully determined.

At point P_1, the value of $\sigma_{\xi\xi}$ is found from the polar stress components, that is,

$$\sigma_{\xi\xi} = \frac{\sigma_{rr} + \sigma_{\theta\theta}}{2} + \frac{\sigma_{rr} - \sigma_{\theta\theta}}{2} \cos\left[2(\phi - \theta)\right] + \sigma_{r\theta} \sin\left[2(\phi - \theta)\right].$$

Substituting the values of polar stresses at point P_1 from Section 3.3 yields

$$\sigma_{\xi\xi} = -p + \frac{\tau}{\sin(2\phi)} - \frac{\tau\cos(2\theta_{p1})}{\sin(2\phi)}\cos\left[2(\phi-\theta)\right] + \frac{\tau\sin(2\theta_{p1})}{\sin(2\phi)}\sin\left[2(\phi-\theta)\right], \tag{5}$$

where θ_{p1}, which is related to the position of $R_1(r,\theta)$, can be expressed as

$$\theta_{p1} = \arctan\left[r(\sin\theta - \sqrt{2}\cos\theta) + \sqrt{2}\right].$$

Similarly, at point Q_1, the value of $\sigma_{\eta\eta}$ can be expressed as

$$\sigma_{\eta\eta} = \frac{\sigma_{rr}+\sigma_{\theta\theta}}{2} + \frac{\sigma_{rr}-\sigma_{\theta\theta}}{2}\cos\left[2(\phi-\theta)\right] - \sigma_{r\theta}\sin\left[2(\phi-\theta)\right].$$

Substituting the polar stresses at point Q_1 from Section 3.3 gives

$$\sigma_{\eta\eta} = -p + \frac{\tau}{\sin(2\phi)} + \frac{\tau\cos(2\theta_{q1})}{\sin(2\phi)}\cos\left[2(\phi-\theta)\right] - \frac{\tau\sin(2\theta_{q1})}{\sin(2\phi)}\sin\left[2(\phi-\theta)\right], \tag{6}$$

where

$$\theta_{q1} = \arctan\left[r\left(\sin\theta + \frac{\cos\theta}{\sqrt{2}}\right) - \frac{1}{\sqrt{2}}\right]. \tag{7}$$

If the yield condition holds in stress zone 1, the stress component $\sigma_{\xi\eta} = \tau$.

3.4. ***Stress zone 2.*** This stress zone shares its β-line with stress zone 1, as illustrated in Figure 6. According to the slip line theory, the stress component $\sigma_{\eta\eta}$ in the two zones takes the same form, that is, Equation (6). To find $\sigma_{\xi\xi}$ in stress zone 2, we use the yield condition along line $\theta = 0^+$ because the α-line intercepts the abscissa.

The boundary line $\theta = 0^+$ in physical space maps to the rotated stress space point C^*. From the rotated yield surface as shown in Figure 6, the relationship between $\sigma_{\xi\xi}$ and $\sigma_{\eta\eta}$ at any boundary point, P_2 is

$$\frac{\sigma_{\xi\xi}(r^*, 0^+) - \sigma_{\eta\eta}(r^*, 0^+)}{2\tau} = \frac{1}{2\sqrt{2}}. \tag{8}$$

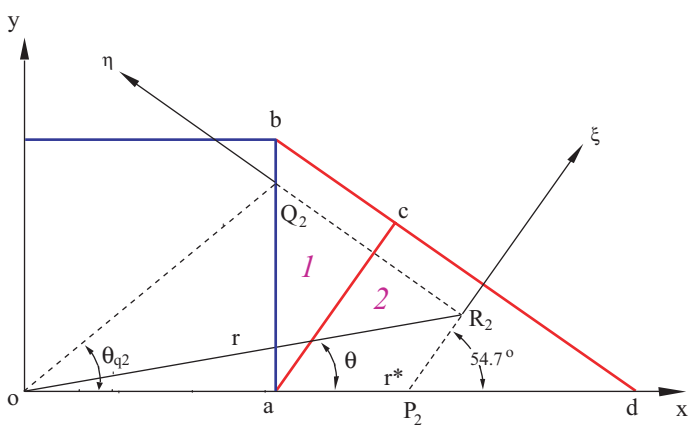

Figure 6. Drawing for finding stress in stress zone 2.

Rearranging this yields

$$\sigma_{\xi\xi}(r^*, 0^+) = \sigma_{\eta\eta}(r^*, 0^+) + \frac{\tau}{\sqrt{2}}. \tag{9}$$

$\sigma_{\eta\eta}(r^*, 0^+)$ can be found from Equation (6) by setting $\theta = 0^+$ and replacing θ_{q1} by $\theta_{q2} = \theta_{q1}(r^*, 0^+)$:

$$\sigma_{\eta\eta}(r^*, 0^+) = -p + \frac{\tau}{\sin(2\phi)} + \tau\cot(2\phi)\cos(2\theta_{q2}) - \tau\sin(2\theta_{q2}), \tag{10}$$

where θ_{q2} is related to r^*, which can be determined from Equation (7) as

$$\theta_{q2} = \arctan\left[\frac{1}{\sqrt{2}}(r^* - 1)\right]. \tag{11}$$

Substituting Equation (10) into Equation (9) yields

$$\sigma_{\xi\xi}(r^*, 0^+) = -p + \frac{\tau}{\sin(2\phi)} + \tau\cot(2\phi)\cos(2\theta_{q2}) - \tau\sin(2\theta_{q2}) + \frac{\tau}{\sqrt{2}}.$$

To find the stress state inside the entire region defined as stress zone 2, we apply the variation method. This is done by expressing r^* and θ_{q2} as functions of r and θ. With respect to Figure 6, if the boundary point $P_2(r^*, 0^+)$ goes into stress zone 2, the law of sines requires

$$r^* = r\frac{\sin(\phi - \theta)}{\sin\phi} = \frac{\sqrt{3}r}{\sqrt{2}}\sin(\phi - \theta). \tag{12}$$

The general form of θ_{q2} follows from Equation (11) and Equation (12), that is,

$$\theta_{q2} = \arctan\left[\frac{\sqrt{3}r}{2}\sin(\phi - \theta) - \frac{1}{\sqrt{2}}\right].$$

Therefore, the stress state in stress zone 2 is

$$\begin{aligned}
\sigma_{\xi\xi} &= -p + \frac{\tau}{\sin(2\phi)} + \tau\cot(2\phi)\cos(2\theta_{q2}) - \tau\sin(2\theta_{q2}) + \frac{\tau}{\sqrt{2}},\\
\sigma_{\eta\eta} &= -p + \frac{\tau}{\sin(2\phi)} + \frac{\tau\cos(2\theta_{q1})}{\sin(2\phi)}\cos\left[2(\phi - \theta)\right] - \frac{\tau\sin(2\theta_{q1})}{\sin(2\phi)}\sin\left[2(\phi - \theta)\right],\\
\sigma_{\xi\eta} &= \tau.
\end{aligned}$$

3.5. ***Stress zone (3).*** According to Figure 7, stress zone 3 and stress zone 1 share the same α-line and also the stress component $\sigma_{\xi\xi}$. To find the stress component $\sigma_{\eta\eta}$, we use the yield condition along the boundary line $\theta = \pi/4$. The yield condition is mapped from the point D^* on the rotated yield surface and can be expressed as

$$\frac{\sigma_{\xi}(r^{**}, \pi/4) - \sigma_{\eta\eta}(r^{**}, \pi/4)}{2\tau} = -2\sqrt{2}.$$

From this and Equation (5), $\sigma_{\eta\eta}(r^{**}, \pi/4)$ can be found by setting $\theta = \pi/4$ and $\theta_{p1} = \theta_{p3}$ as

$$\sigma_{\eta\eta}(r^{**}, \frac{\pi}{4}) = -p + \frac{\tau}{\sin(2\phi)} - \frac{\tau\cos(2\theta_{p3})}{\sin(2\phi)}\cos\left[2(\phi - \frac{\pi}{4})\right] + \frac{\tau\sin(2\theta_{p3})}{\sin(2\phi)}\sin\left[2(\phi - \frac{\pi}{4})\right] + 4\sqrt{2}\tau, \tag{13}$$

where θ_{p3} is θ_{p1} at $r = r^{**}$ and $\theta = \pi/4$, that is,

$$\theta_{p3} = \arctan\left[r^{**}\left(\frac{1}{\sqrt{2}} - 1\right) + \sqrt{2}\right]. \tag{14}$$

Noting that $\phi = 54.7°$, Equation (13) simplifies to

$$\sigma_{\eta\eta}(r^{**}, \frac{\pi}{4}) = -p + \frac{\tau}{\sin(2\phi)} - \frac{2\sqrt{2}\tau\cos(2\theta_{p3})}{3\sin(2\phi)} + \frac{\tau\sin(2\theta_{p3})}{3\sin(2\phi)} + 4\sqrt{2}\tau.$$

To extend the stress solutions to the entire stress zone 3, r^{**}, as a function of r and θ, becomes, by the law of sines,

$$r^{**} = \frac{\sqrt{2}r}{1+\sqrt{2}}(\cos\theta + \sqrt{2}\sin\theta). \tag{15}$$

Therefore, the stress state in stress zone 3 is

$$\begin{aligned}
\sigma_{\xi\xi} &= -p + \frac{\tau}{\sin(2\phi)} - \frac{\tau\cos(2\theta_{p1})}{\sin(2\phi)}\cos[2(\phi-\theta)] + \frac{\tau\sin(2\theta_{p1})}{\sin(2\phi)}\sin[2(\phi-\theta)],\\
\sigma_{\eta\eta} &= -p + \frac{\tau}{\sin(2\phi)} - \frac{2\sqrt{2}\tau\cos(2\theta_{p3})}{3\sin(2\phi)} + \frac{\tau\sin(2\theta_{p3})}{3\sin(2\phi)} + 4\sqrt{2}\tau,\\
\sigma_{\xi\eta} &= \tau.
\end{aligned}$$

The general form of θ_{p3} follows from substituting r^{**} in (15) into (14):

$$\theta_{p3} = \arctan\left[\sqrt{2} - r(\cos\theta + \sqrt{2}\sin\theta)(3 - 2\sqrt{2})\right].$$

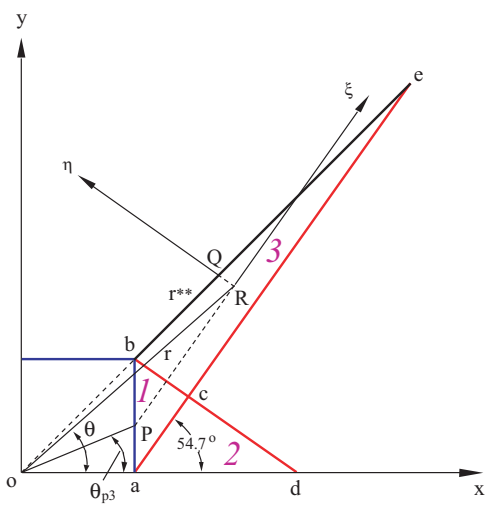

Figure 7. Drawing for finding stress in stress zone 3.

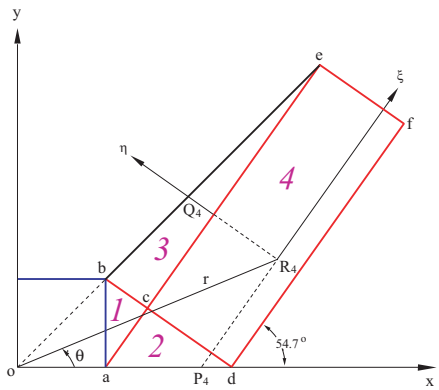

Figure 8. Drawing for finding stress in stress zone 4.

3.6. ***Stress zone 4.*** The analysis of this zone (and the next) is very much like that of stress zone 3. According to Figure 8, stress zone 4 and stress zone 2 share the same α-line and $\sigma_{\xi\xi}$. Also, stress zone 4 and stress zone 3 share the same β-line, and thus $\sigma_{\eta\eta}$ as well. Therefore, the stress state in stress zone 4 can be obtained as

$$\begin{aligned}
\sigma_{\xi\xi} &= -p + \frac{\tau}{\sin(2\phi)} + \tau\cot(2\phi)\cos(2\theta_{q2}) - \tau\sin(2\theta_{q2}) + \frac{\tau}{\sqrt{2}},\\
\sigma_{\eta\eta} &= -p + \frac{\tau}{\sin(2\phi)} - \frac{2\sqrt{2}\tau\cos(2\theta_{p3})}{3\sin(2\phi)} + \frac{\tau\sin(2\theta_{p3})}{3\sin(2\phi)} + 4\sqrt{2}\tau,\\
\sigma_{\xi\eta} &= \tau.
\end{aligned} \tag{16}$$

3.7. ***Stress zone 5.*** From Figure 9, stress zone 5 and stress zone 4 share a β-line and $\sigma_{\eta\eta}$ in the form given by Equation (16). To find $\sigma_{\xi\xi}$ in stress zone 5, we use the same method as used for finding $\sigma_{\xi\xi}$ in stress zone 2. We apply the yield condition along line $\theta = 0^+$, as shown in Equation (8), for establishing the relationship between $\sigma_{\xi\xi}$ and $\sigma_{\eta\eta}$ at any point on this boundary.

We define a new parameter $\theta_{p5} = \theta_{p3}(r^*, 0^+)$ for deriving $\sigma_{\xi\xi}$ in this zone, that is,

$$\theta_{p5} = \arctan\left[\sqrt{2} - r^*(3 - 2\sqrt{2})\right].$$

A more general form of θ_{p5} for points inside the stress zone is

$$\theta_{p5} = \arctan\left[\sqrt{2} - \frac{3 - 2\sqrt{2}}{\sqrt{2}}\, r(\sqrt{2}\cos\theta - \sin\theta)\right].$$

The stress state in stress zone 5 is

$$\sigma_{\xi\xi} = -p + \frac{\tau}{\sin(2\phi)} - \frac{2\sqrt{2}\tau}{3\sin(2\phi)}\cos(2\theta_{p5}) + \frac{\tau\sin(2\theta_{p5})}{\sin(2\phi)} + \frac{\tau}{\sqrt{2}} + 4\sqrt{2}\tau,$$
$$\sigma_{\eta\eta} = -p + \frac{\tau}{\sin(2\phi)} - \frac{2\sqrt{2}\tau\cos(2\theta_{p3})}{3\sin(2\phi)} + \frac{\tau\sin(2\theta_{p3})}{3\sin(2\phi)} + 4\sqrt{2}\tau,$$
$$\sigma_{\xi\eta} = \tau.$$

3.8. ***Stress zone 6.*** The procedures for finding the stresses in stress zone 6 are the same those for stress zone 3. Stress zone 6 and stress zone 4 share the an α-line and $\sigma_{\xi\xi}$. The stress component $\sigma_{\eta\eta}$ is found from the yield condition along the boundary line $\theta = \pi/4$, which is shown in Section 3.5.

For the points on the boundary $\theta = \pi/4$, we define θ_{q6}, a function of r^{**}, as

$$\theta_{q6} = \arctan\left(\frac{\sqrt{2}-1}{2}r^{**} - \frac{1}{\sqrt{2}}\right).$$

For the points within stress zone 6, θ_{q6} is a function of r and θ, that is,

$$\theta_{q6} = \arctan\left(\frac{3\sqrt{2}-4}{2}r(\cos\theta + \sqrt{2}\sin\theta) - \frac{1}{\sqrt{2}}\right).$$

Therefore, the stress state in stress zone 6 is given by

$$\sigma_{\xi\xi} = -p + \frac{\tau}{\sin(2\phi)} + \tau\cot(2\phi)\cos(2\theta_{q2}) - \tau\sin(2\theta_{q2}) + \frac{\tau}{\sqrt{2}},$$
$$\sigma_{\eta\eta} = -p + \frac{\tau}{\sin(2\phi)} + \tau\cot(2\phi)\cos(2\theta_{q6}) - \tau\sin(2\theta_{q6}) + \frac{\tau}{\sqrt{2}} + 4\sqrt{2}\tau,$$
$$\sigma_{\xi\eta} = \tau.$$

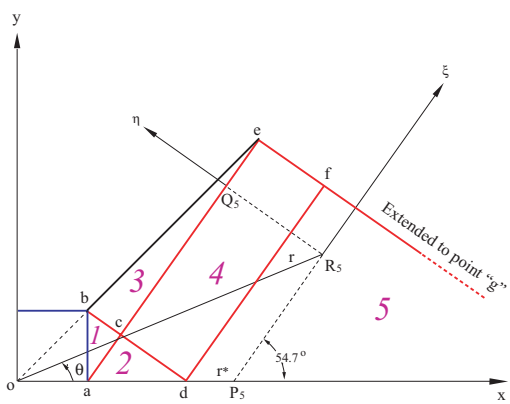

Figure 9. Drawing for finding stress in stress zone 5.

4. Results and discussion

4.1. ***Stress along circumferential paths.*** The analytical solutions in the region $0 \le \theta \le 45°$, as presented in Sections 3.3 to Section 3.8, provide for obtaining the stress field around the microchannel through a series of mapping operations along special symmetrical lines. The first mapping is that the solutions in $0 \le \theta \le 45°$ can be reflected over the line $\theta = 45°$ to get the solutions in $45° \le \theta \le 90°$. The solution from $0 \le \theta \le 90°$ can be translated 90° for solving in $90° \le \theta \le 180°$. Once we know the stress around the upper half of the channel, the values in lower half plane follow from reflection across x-axis.

In the following discussion, the half width of the microchannel is defined as $w_\circ$. To show the stress solutions quantitatively and for simplicity, we set to unity the half width of the channel. We also set τ to unity, and the internal pressure becomes

$$p = \frac{\tau}{\sin\phi\cos\phi} = \frac{3}{\sqrt{2}},$$

which is the critical value for initiation yielding at the boundary point O of Figure 1.

Figure 10 and Figure 11 show the stress state along circumferential paths in the angular range $0 \le \theta \le 180°$. Figure 10 depicts the stresses along the path $r/w_\circ = r_b/w_\circ = \sqrt{2}$. There, the stresses are normalized by the critical shear strength τ. Figure 10a shows the stress components in the local ξ-η coordinate system. The normal stresses $\sigma_{\xi\xi}$ and $\sigma_{\eta\eta}$ show jump abruptly $\theta = 45°$ and $\theta = 135°$. Nevertheless, the most rapid change in the shear stress $\sigma_{\xi\eta}$ occurs at $\theta = 90°$.

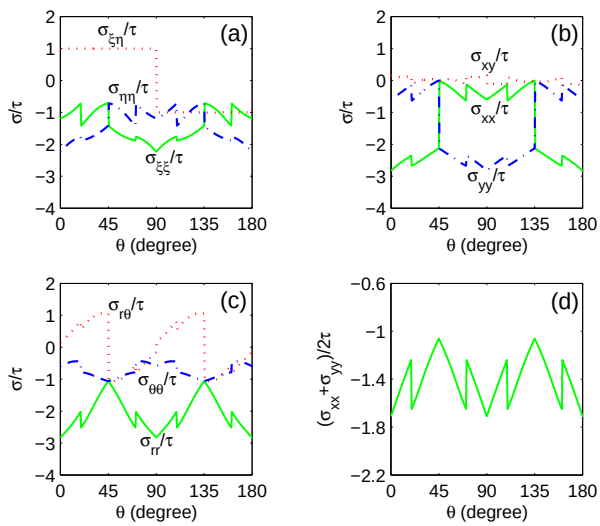

Figure 10. Stress state around the circumferential path $r/w_\circ = r_b/w_\circ = \sqrt{2}$: (a) normalized stress components in the local ξ-η coordinates, (b) normalized stress components in x-y Cartesian coordinates, (c) normalized stress components in r-θ polar coordinates, (d) the normalized out-of-plane stress component.

Figure 10b shows the stresses in the x-y Cartesian coordinates. The shear stress σ_{xy} is almost equal to zero, which is reasonable because the circumferential path is very close to the inner wall of the microchannel. On the inner wall of the channel, the nonshear boundary condition holds. By the same logic, the numerical values of normal stresses σ_{xx} and σ_{yy} also recover the boundary conditions. For example, in the angular ranges $0 \le \theta \le 45°$ and $135° \le \theta \le 180°$, $\sigma_{xx} \approx -p = -3/\sqrt{2}$, and $\sigma_{yy} \approx 0$, which means that material near the two vertical walls of the microchannels is under a horizontal pressure of about $-p$. Nevertheless, in the range $45° \le \theta \le 135°$, $\sigma_{xx} \approx 0$ and $\sigma_{yy} \approx -p = -3/\sqrt{2}$, indicating that material close to the top horizontal wall of the microchannel undergoes a vertical compressive pressure of about $-p$.

In polar coordinates, the shear stress $\sigma_{r\theta}$ changes abruptly at $\theta = 45°$ and $\theta = 135°$, as shown in Figure 10c. $\sigma_{r\theta}$ is a periodic function with period 90°. The radial and hoop stress components, σ_{rr} and $\sigma_{\theta\theta}$, are also 90°-periodic functions. In addition, they show mirror symmetry about the line $\theta = 90°$. Figure 10d shows how the the trace of the stresses changes along the angular path. Under the assumed isochoric condition, the trace of the stresses is equal to the out-of-plane stress.

We also examine the stress solutions along another two circumferential paths,

$$r/w_\circ = (r_b + r_c)/(2w_\circ) \approx 1.52 \quad \text{and} \quad r/w_\circ = r_c/w_\circ = \sqrt{5 + 2\sqrt{2}}/\sqrt{3} \approx 1.62.$$

The stresses along these two constant-radius lines show the same trend, that is, the stress state is nonuniform, resulting in anisotropic deformation of material around the microchannel. Another common feature which can be seen from the results is that all stress components except for $\sigma_{\xi\eta}$ peak either along the lines

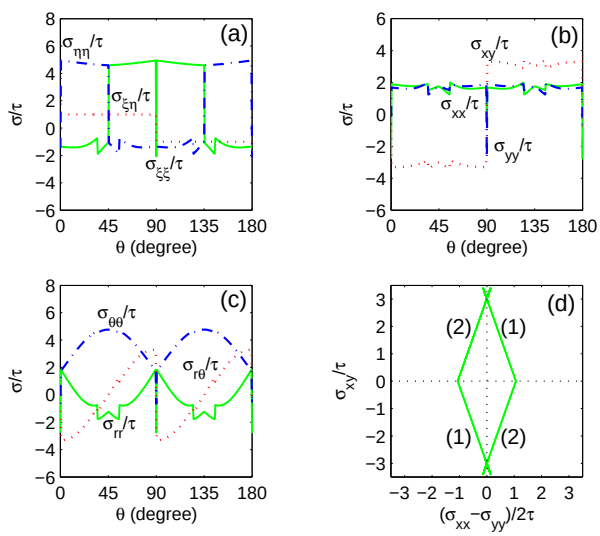

Figure 11. Stress state around the circumferential path $r/w_\circ = r_d/w_\circ = 1 + \sqrt{2}$: (a) normalized stress components in the local ξ-η coordinates, (b) normalized stress components in x-y Cartesian coordinates, (c) normalized stress components in r-θ polar coordinates, (d) yield surface.

$\theta = 45°$ and $\theta = 135°$ or close to these lines. Evidently, the regions containing the radial lines $\theta = 45°$ and $\theta = 135°$ experience higher loading than elsewhere, and we expect intense shear deformation along these two lines. This agrees with the slip model shown in Figure 1.

Figure 11 shows the stress state along the path, $r/w_\circ = r_d/w_\circ = 1+\sqrt{2}$. The stress field is not uniform along this path, which indicates an anisotropic deformation state. Specifically, Figure 11d illustrates the yield surface along the path. The plastic deformation there comes from the active slip of the two slip systems marked (1) and (2). Obviously, Figure 11d recovers well the yield conditions from the analytical model of plasticity in Section 2.2 and shown in Figure 3b. We note that the line $\theta = 45°$ is the boundary for slip system 1 and slip system 2. Similarly, $\theta = 135°$ is also a slip sector boundary. These are the places where stress concentrates before yielding due to the corner effect. Material on these boundaries can flow along either slip system 1 or slip system 2. Thus, the yield surface bifurcates at the intercept points on the vertical axis in Figure 11d.

4.2. ***Stress maps.*** In this section, we present the stress maps of microneedles containing square microchannels. These have potential applications for cell registration, fluid injection, and nanofiber synthesis. As a case study, we choose a cylindrical microneedle with radius $r/w_\circ = r_e/w_\circ = 2+2\sqrt{2} \approx 4.83$. $w_\circ$ is the microchannel half-width, as defined in Section 4.1. The channel itself is centered in the cylindrical needle. We assume here that internal pressure controls the deformation. Thus, the boundary conditions for stresses on the inside wall propagate in material around the channel along the characteristics (slip-lines). The assumption is reasonable for cases such as confined growth of nanofibers within the channel, fluid injection from the channel, and cell registration under suction by internal pressure.

Figure 12 shows stress zones in the needle around the microchannel, which exhibit the expected four-fold symmetry. Figures 13–16 show stress maps in different coordinate systems and various other features, as discussed below.

Figure 13 maps the normalized radial stress σ_{rr}/τ; the map reveals evenly distributed compressive regions near the inner wall of the channel. These compressive regions propagate along the slip sector

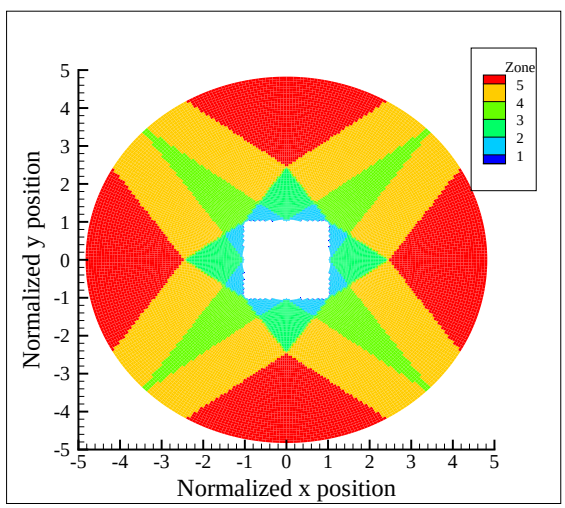

Figure 12. Contour plot showing the stress zones around the microchannel.

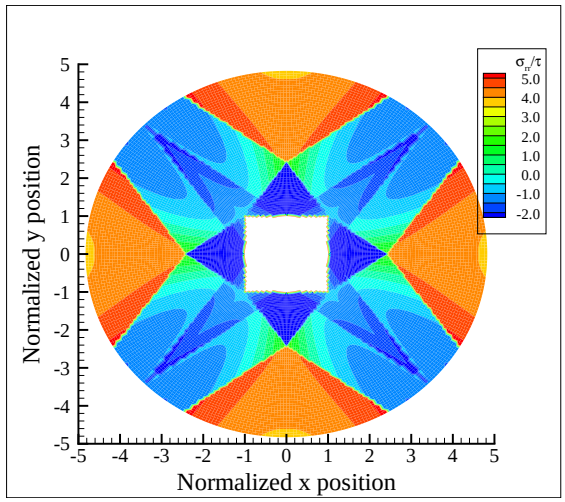

Figure 13. Contour map showing the normalized polar stress σ_{rr}/τ around the microchannel.

boundaries, that is, along multiples of $\theta = \pi/4$. The compressed regions are separate from the regions under intense tension away from the channel. The normalized hoop stress $\sigma_{\theta\theta}/\tau$, shown in Figure 14, shows a similar compressed region near the channel's inner wall. However, close to the outer boundary of the microneedle, the $\sigma_{\theta\theta}/\tau$ implies a tension state. On the map of normalized polar shear stress ($\sigma_{r\theta}/\tau$ in Figure 15), we see neutral zones around the channel. Away from the channel and along circumferential paths — for example, at $r/w_\circ = 1 + \sqrt{2}$ — the stress state alternates between compression and tension.

We can also examine in the x-y global Cartesian coordinate system the stress maps for σ_{xx}/τ and σ_{yy}/τ. They exhibit discrete tension and compression zones. The inner boundary conditions propagate in the stress zones adjacent to the inner wall. For example, we find $\sigma_{xx} = -p$ in $0 \le \theta \le 45°$ within the

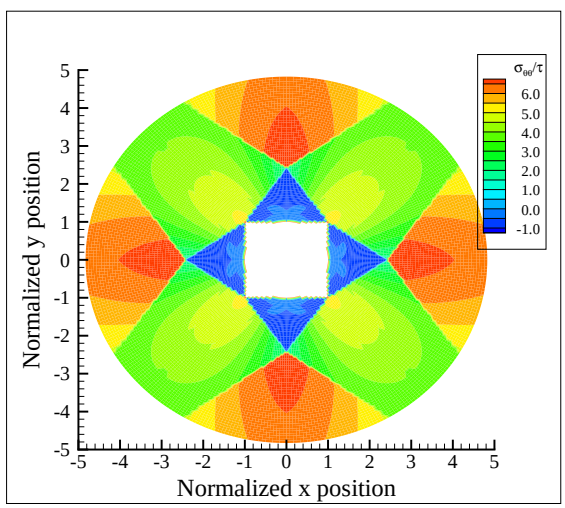

Figure 14. Contour map showing the normalized polar stress $\sigma_{\theta\theta}/\tau$ around the microchannel.

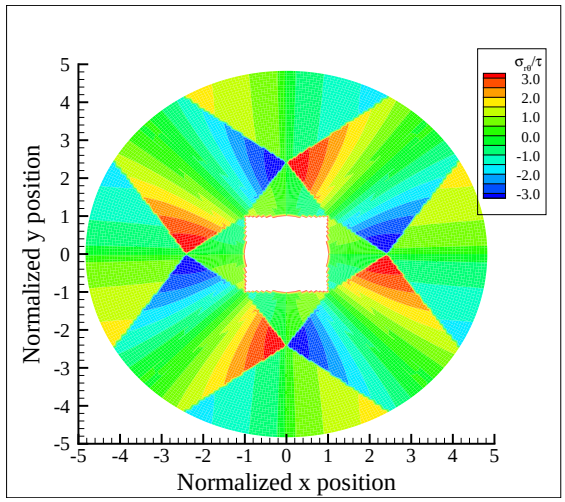

Figure 15. Contour map showing the normalized polar stress $\sigma_{r\theta}/\tau$ around the microchannel.

zone containing the channel's vertical wall, while $\sigma_{yy} = -p$ in $45° \leq \theta \leq 90°$ within the zone horizontal wall. Tension stress states occupy the region near to the outer boundary of the microneedle. We note that the map σ_{yy}/τ is just σ_{xx}/τ rotated by $\pi/2$. On the map for normalized shear stress σ_{xy}/τ, the inner wall satisfies the nonshear condition. The nonshear zones are located along both the x- and y-axis. The shear zones appear at multiples of $\theta = \pi/4$.

Figure 16 shows, in the ξ-η local Cartesian coordinate system, the stress maps for $\sigma_{\xi\xi}/\tau$. Obviously, the $\sigma_{\eta\eta}/\tau$ map can be obtained by rotating the figure by $\pi/2$. In this map, the normalized stress $\sigma_{\xi\xi}/\tau$ is constant along the characteristics, or α-lines. Similarly, $\sigma_{\eta\eta}/\tau$ is constant along β-lines. This agrees with the predictions of slip line theory. In the local coordinate system, the normalized shear stress $\sigma_{\xi\eta}/\tau$ stays

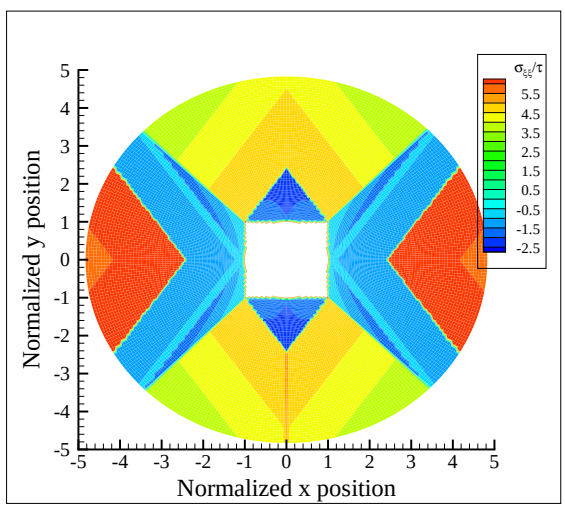

Figure 16. Contour map showing the normalized stress $\sigma_{\xi\xi}/\tau$ in the local ξ-η Cartesian coordinates.

constant in each quadrant, revealing the anisotropic plasticity of the material. The results also indicate the deformation behavior of global yielding without any strain hardening.

We can also look at the trace of the stresses. In the plane, the trace is related to pressure; out of the plane, it represents stress under isochoric conditions. The trace results show the nonuniform distributions in the in-plane pressure and the out-of-plane stress. Finally, we examine the normalized in-plane stress difference $(\sigma_{xx} - \sigma_{yy})/(2\tau)$, which is the stress measure on the stress space abscissa. This difference shows symmetrically distributed zones. The stress maps of Figures 12–16 reveal the nonuniform stress states to be as predicted by the analytical solutions in Section 3, namely, that materials containing microchannels under internal pressure exhibit anisotropic plastic deformation.

We stress that the model here is an idealized and simplified one which provides some preliminary results. For more sophisticated material models, it is difficult to obtain closed form solutions, and only numerical solutions may be available. Thus, subsequent finite element simulations should be implemented to treat real world problems with different strain hardening laws. Because analytical solutions can only be obtained from simplified models that assume an ideally rigid plastic solid, this work may be considered as a good starting point for tackling more complicated cases. Already underway are systematic finite element simulations of microchannels with different geometrical configurations shaped like as squares, circles, cylinders, and ellipses; these are based on material models with a prescribed elastic-plastic constitutive relation. Using the preliminary results presented in this work, it may be possible to compare the analytical predictions with numerical ones.

Another issue facing the practical applications is the stress concentration problem. Typically, stress concentrates at sharp corners and cracks. In this model, stress will concentrate at the four microchannel corners with $\theta = \pi/4$, $3\pi/4$, $5\pi/4$, and $7\pi/4$. Stress concentrations cause the material to yield at a lower overall stress level. Thus, the yield surface will contract and the points B and D shown in Figure 3a will move towards the origin. Consequently, the yield surface will change from a diamond to a more complex shape. The stress zones would need to be redefined and the processes for seeking the analytical solutions to the stresses would be more complicated. In the end, finite element simulations may be the proper way to deal with the stress concentration issue.

5. Conclusions

From our studies of the stress states around microchannels under internal compressive loading, the following conclusions can be made.

First, the simplified yielding model can be used to characterize the plastic flow in materials containing microchannels. When the material is under strain deformation conditions, the model allows identification of slip bands around the channels.

Second, we can obtain closed form solutions to stress fields around the microchannels. The solutions hold in both the zones containing and those away from the inner boundary. The stress distributions are nonuniform. The results predict anisotropic deformation states around the channels.

Third, we determine the yield conditions associated with the plastic flow along different slip bands. From the yield surface along circumferential paths, it is found that, at the corner of the square-shaped microchannel, two slip systems have the same chance of being activated.

Finally, the stress maps of microneedles containing square microchannels reveal discrete isostress zones and predict anisotropic plastic deformation of the material around the channels.

References

[Allen 2005] J. J. Allen, *Micro electro mechanical system design*, Taylor and Francis, Boca Raton, FL, 2005.

[Fleck et al. 1994] N. A. Fleck, G. M. Muller, M. F. Ashby, and J. W. Hutchinson, "Strain gradient plasticity:theory and experiment", *Acta Metall. Mater.* **42**:2 (1994), 475–487.

[Franssila 2004] S. Franssila, *Introduction to microfabrication*, J. Wiley, New York, 2004.

[Gan and Kysar 2007] Y. X. Gan and J. W. Kysar, "Cylindrical void in a rigid-ideally plastic single crystal, III: hexagonal close-packed crystal", *Int. J. Plasticity* **23**:4 (2007), 592–619.

[Gan et al. 2006] Y. X. Gan, J. W. Kysar, and T. L. Morse, "Cylindrical void in a rigid-ideally plastic single crystal, II: experiments and simulations", *Int. J. Plasticity* **22**:1 (2006), 39–72.

[Hill 1998] R. Hill, *The mathematical theory of plasticity*, Oxford University Press, New York, 1998.

[Huang et al. 1991] Y. Huang, J. W. Hutchinson, and V. Tvergaard, "Cavitation instabilities in elastic-plastic solids", *J. Mech. Phys. Solids* **39**:2 (1991), 223–241.

[Hwang and Song 2007] H.-S. Hwang and J.-T. Song, "An effective method to prevent stiction problems using a photoresist sacrificial layer", *J. Micromech. Microeng.* **17**:2 (2007), 245–249.

[Kysar et al. 2005] J. W. Kysar, Y. X. Gan, and G. Mendez-Arzuza, "Cylindrical void in a rigid-ideally plastic single crystal, I: anisotropic slip line theory solution for face-centered cubic crystals", *Int. J. Plasticity* **21**:8 (2005), 1481–1520.

[Lee et al. 2003] N. K. S. Lee, G. H. Yu, J. Y. Chen, and A. Joneja, "Effect of mechanical alignment system on assembly accuracy", *J. Manuf. Sci. Eng.* (*Trans. ASME*) **125**:3 (2003), 595–608.

[Li et al. 2004] B. Li, H. Yu, A. Sharon, and X. Zhang, "Rapid three-dimensional manufacturing of microfluidic structures using a scanning laser system", *Appl. Phys. Lett.* **85**:12 (2004), 2426–2428.

[Lu et al. 2007] Z. Lu, P. C. Y. Chen, J. Nam, R. Ge, and W. Lin, "A micromanipulation system with dynamic force-feedback for automatic batch microinjection", *J. Micromech. Microeng.* **17**:2 (2007), 314–321.

[Lubarda et al. 2004] V. A. Lubarda, M. S. Schneider, D. H. Kalantar, B. A. Remington, and M. A. Meyers, "Void growth by dislocation emission", *Acta Mater.* **52**:6 (2004), 1397–1408.

[Nadai 1950] A. Nadai, *Theory of flow and fracture of solids*, McGraw-Hill, New York, 1950.

[Needleman and Tvergaard 1991] A. Needleman and V. Tvergaard, "A numerical study of void distribution effects on dynamic, ductile crack growth", *Eng. Fract. Mech.* **38**:2-3 (1991), 157–173.

[O'Regan et al. 1997] T. L. O'Regan, D. F. Quinn, M. A. Howe, and P. E. McHugh, "Void growth simulations in single crystals", *Comput. Mech.* **20**:1-2 (1997), 115–121.

[Rice 1973] J. R. Rice, "Plane strain slip line theory for anisotropic rigid/plastic materials", *J. Mech. Phys. Solids* **21**:2 (1973), 63–74.

[Rice and Tracey 1969] J. R. Rice and D. M. Tracey, "On the ductile enlargement of voids in triaxial stress fields", *J. Mech. Phys. Solids* **17**:3 (1969), 201–217.

[Schacht et al. 2003] T. Schacht, N. Untermann, and E. Steck, "The influence of crystallographic orientation on the deformation behavior of single crystals containing microvoids", *Int. J. Plasticity* **19**:10 (2003), 1605–1626.

[Senturia 2001] S. D. Senturia, *Microsystem design*, Kluwer Academic, Boston, 2001.

[Timpe and Komvopoulos 2006] S. J. Timpe and K. Komvopoulos, "The effect of adhesion on the static friction properties of sidewall contact interfaces of microelectromechanical devices", *J. Microelectromech. S.* **15**:6 (2006), 1612–1621.

[Tseng et al. 2002a] F.-G. Tseng, C.-J. Kim, and C.-M. Ho, "A high-resolution high-frequency monolithic top-shooting microinjector free of satellite drops ¨CPart I: Concept, design, and model", *J. Microelectromech. S.* **11**:5 (2002), 427–436.

[Tseng et al. 2002b] F.-G. Tseng, C.-J. Kim, and C.-M. Ho, "A high-resolution high-frequency monolithic top-shooting microinjector free of satellite drops ¨CPart II: Fabrication, implementation, and characterization", *J. Microelectromech. S.* **11**:5 (2002), 437–447.

[Tvergaard 1991] V. Tvergaard, "Failure by ductile cavity growth at a metal-ceramic interface", *Acta Metall. Mater.* **39**:3 (1991), 419–426.

[Tvergaard and Hutchinson 2002] V. Tvergaard and J. W. Hutchinson, "Two mechanisms of ductile fracture: void by void growth versus multiple void interaction", *Int. J. Solids Struct.* **39**:13-14 (2002), 3581–3597.

[Tvergaard and Niordson 2004] V. Tvergaard and C. Niordson, "Nonlocal plasticity effects on interaction of different size voids", *Int. J. Plasticity* **20**:1 (2004), 107–120.

[Yu et al. 2004] H. Yu, O. Balogun, B. Li, T. W. Murray, and X. Zhang, "Building embedded microchannels using a single layered SU-8 and determining Young's modulus using a laser acoustic technique", *J. Micromech. Microeng.* **14**:11 (2004), 1576–1584.

[Yu et al. 2006a] H. Yu, O. Balogun, B. Li, T. W. Murray, and X. Zhang, "Fabrication of three-dimensional microstructures based on single-layered SU-8 for lab-on-chip applications", *Sensor. Actuat. A Phys.* **127**:2 (2006), 228–234.

[Yu et al. 2006b] H. Yu, B. Li, and X. Zhang, "Flexible fabrication of three-dimensional multi-layered microstructures using a scanning laser system", *Sensor. Actuat. A Phys.* **125**:2 (2006), 553–564.

[Zhe et al. 2007] J. Zhe, A. Jagtiani, P. Dutta, J. Hu, and J. Carletta, "A micromachined high throughput Coulter counter for bioparticle detection and counting", *J. Micromech. Microeng.* **17**:2 (2007), 304–313.

[Ziegler et al. 2006] D. Ziegler, T. Suzuki, and S. Takeuchi, "Fabrication of flexible neural probes with built-in microfluidic channels by thermal bonding of parylene", *J. Microelectromech. S.* **15**:6 (2006), 1477–1482.

Received 2 Apr 2007. Accepted 11 Jun 2007.

YONG XUE GAN: yong.gan@utoledo.edu
Department of Mechanical, Industrial and Manufacturing Engineering College of Engineering, University of Toledo, Toledo, OH 43606, United States